Electromagnetic modeling of PMSM based on multi-scale physics-informed neural network with dual-level Bayesian uncertainty weighting mechanism

Jiewei Lu[1,2], Dian Zhang[1], Peixin Liang[1], Yong Zhao[1], and Guangzhao Luo[2*]

***Abstract*— Accurate estimation of electromagnetic responses in permanent magnet synchronous motors (PMSMs) is crucial for complex engineering applications. Therefore, a multi-scale physics-informed neural network (M-BPINN) with a dual-level Bayesian uncertainty weighting mechanism is proposed. Discrete spatial scaling and periodic sinusoidal representation networks (SIRENs) are utilized by the multi-scale architecture to ensure that high-frequency spatial features are accurately captured. The adaptive weighting mechanism based on Bayesian uncertainty will automatically evaluate the reliability of constraints to reduce gradient stiffness. The evaluation was conducted on the simulation model of an 8-pole 54 slot conical rotor permanent magnet synchronous motor, the relative average absolute error (RelMAE) of magnetic vector potential A_z is less than 2.5%, and the RelMAE of magnetic flux density B and field strength H is 7%–13%, demonstrating improved accuracy compared to traditional methods. Furthermore, computational speed is accelerated by three orders of magnitude by this model. It is demonstrated that significant potential for real-time control and digital twin applications.**

I. INTRODUCTION

Accurate estimation of the electromagnetic response in permanent magnet synchronous motors (PMSMs) is critical for complex engineering applications, including aerospace, electric vehicles, and intelligent robots [1]. Especially, special topology motors such as conical rotor permanent magnet synchronous motors (CR-PMSMs) are increasingly being used in aerospace electric propulsion systems, exhibiting significant nonlinear characteristics due to their air gap geometry and cone angle related magnetic flux distribution [2]. Variations in rotor position and load conditions dynamically alter the electromagnetic parameters during operation, increasing the difficulty of modeling [3]. Traditional mathematical models are difficult to capture these coupled nonlinearities, although finite element analysis (FEA) provides high solution accuracy and physical consistency, but the computational cost on dense grids is high, and the grid quality depends on human expertise, which limits its applicability to digital twin or real time control scenarios [4], [5].

*This work was supported by the Shenzhen Science and Technology Program under Grant GJHZ20240218114402006. This work was also supported in part by the Key Research and Development Program in Shaanxi Province of China under Grant 2025CY-YBXM-081, and in part by the Aeronautical Science Foundation of China under Grant 20240040053003.

[1]Jiewei Lu, Dian Zhang, Peixin Liang, and Yong Zhao are with the School of Automation, Northwestern Polytechnical University, Xi’an 710072, China 2025101279ljw@mail.nwpu.edu.cn, zdrex@mail.nwpu.edu.cn, liang_peixin@nwpu.edu.cn, zhaoyong@nwpu.edu.cn

[2]Jiewei Lu and Guangzhao Luo are with the Shenzhen Research Institute of Northwestern Polytechnical University, Shenzhen 518057, China. Guangzhao Luo is the corresponding author 2025101279ljw@mail.nwpu.edu.cn, guangzhao.luo@nwpu.edu.cn

Data-driven deep learning models facilitate rapid inference [6], [7], [8]. Nevertheless, the extensive training data required to cover all possible normal and fault conditions is often cost-prohibitive and practically unattainable. Therefore, Physical-informed Neural Networks (PINNs) have become a promising solution by incorporating Governing Partial Differential Equations (PDEs) as regularization into the loss function to ensure robust solutions under sparse data conditions [9], [10].

However, the application of conventional PINNs to PMSMs presents two primary challenges [11], [12]. Firstly, inherent spectral bias of neural networks limits the capacity to fit high-gradient, high-frequency spatial magnetic fields. These complex fields are typically generated by intricate geometric boundaries and air gaps [13], [14]. Secondly, optimizing multiple competing loss objectives can lead to gradient imbalance and stiffness [15]. Existing mitigation strategies include empirical weight adjustment, Neural Tangent Kernel (NTK) analysis [16], trainable pointwise weights [17], and hard constraints [18]. These approaches typically generate excessive computational overhead or encounter training difficulties across complex geometries. Numerical noise originating from FEA interpolation errors further degrades the prediction accuracy.

A multi-scale physical information neural network (M-BPINN) with dual-level Bayesian uncertainty weighting mechanism is proposed to address these challenges. The main contributions are as follows:

Firstly, discrete spatial scaling factors and periodic sinusoidal activation functions are incorporated into the multi-scale physics-informed neural network (MPINN). This architecture effectively reduces the spectral bias problem, enabling high-precision fitting of high-gradient spatial magnetic fields at the complex stator-rotor boundaries.

Secondly, a dual-level adaptive loss weighting mechanism based on Bayesian uncertainty estimation is proposed. Homoscedastic uncertainty balances data loss weights at the first level, while a noise-aware sigma weighter handles physical constraints at the second level, automatically assessing constraint reliability and alleviating gradient stiffness.

Finally, a cosine annealing learning rate is combined with a progressive physical constraint activation strategy. This combination ensures smooth convergence and prevents premature local optima.

The rest of this article is structured as follows: Section II describes the proposed methodology, Section III provides a detailed introduction to the experimental setup, Section IV analyzes the results, and Section V summarizes this study.

II. Methodology

This section presents the proposed M-BPINN methodology, comprising three components: Maxwell-equation-based physical constraints (Section II-A), the MPINN architecture (Section II-B), and the dual-level adaptive loss weighting mechanism (Section II-C). The overall architecture is illustrated in Fig. 1.

A. Physical Constraints and Governing Equations

In the full-domain electromagnetic field modeling of PMSMs, the Maxwell equations are embedded as physical constraints in the neural network and converge to the physically feasible solution space. Under this physics-informed architecture, the electromagnetic PDEs are prior regularization term. The Magnetic Vector Potential A_z is the fundamental output of the neural network, and all other electromagnetic quantities are derived from it. Considering the dynamic characteristics during motor operation, the magnetic flux density B are defined in the rotor-rotating coordinate system as follows:

$$B = \nabla \times A \tag{1}$$

In a two-dimensional Cartesian coordinate system, as shown in (2):

$$\begin{aligned} B_x &= \cos(\theta)\frac{\partial A_z}{\partial Y} + \sin(\theta)\frac{\partial A_z}{\partial X} \\ B_y &= \sin(\theta)\frac{\partial A_z}{\partial Y} - \cos(\theta)\frac{\partial A_z}{\partial X} \end{aligned} \tag{2}$$

Where θ represents the rotor mechanical angle, and B_x, B_y represent the magnetic flux densities in the x and y directions, respectively. A supervised physics-informed neural network (PINN) is trained by formulating a strong-form residual loss. This residual ensures that consistency is maintained between the direct predictions of the network (A_z, E_z, B_x, B_y) and the values derived via automatic differentiation through A_z:

$$R_{r1} = (B_x - B_x^{calc}(A_z)) + (B_y - B_y^{calc}(A_z)) \tag{3}$$

Where $B_{x,y}^{calc}$ are automatically differentiated and derived by A_z through (2). Within the air-gap domain, the linear constitutive relation $B = \mu_0 H$ enforces an additional constraint, as shown in (4):

$$R_{r2} = (B_x - \mu_0 H_x) + (B_y - \mu_0 H_y) \tag{4}$$

In addition, considering the relationship between magnetic field strength H and current density J, the strong form of Ampere's law is shown in (5):

$$\nabla \times H = J \tag{5}$$

Since $\mathbf{H}$ is obtained from $\mathbf{B}$, and $\mathbf{B}$ is computed from the magnetic vector potential A_z through $\mathbf{B} = \nabla \times A_z$, directly enforcing (5) requires second-order spatial derivatives of A_z. This may amplify high-frequency noise and cause gradient ill-conditioning problems. Therefore, the variational weak form is adopted by introducing a smooth test function W, the original equation is transformed as shown in (6):

$$\int (H \cdot \nabla \times W) d\Omega - \int (J \cdot W) d\Omega = 0 \tag{6}$$

Where H is the magnetic field intensity and J is the current density. This transfers high-order derivatives from the predicted fields to the predefined test functions. A set of two-dimensional trigonometric functions W_k featuring a scaling parameter R is utilized for this purpose, as shown in (7):

$$W_k(x, y) = \sin\left(\frac{n_x \pi x}{R}\right)\cos\left(\frac{n_y \pi y}{R}\right) \tag{7}$$

where $k = (n_x, n_y)$ denotes the two-dimensional mode index of the test function, and n_x and n_y are the mode numbers in the x- and y-directions, respectively. The variational residual is defined as shown in (8):

$$R_{r3,k} = \int \left(H_x \frac{\partial W_k}{\partial y} - H_y \frac{\partial W_k}{\partial x}\right) d\Omega - \int J_z W_k d\Omega \tag{8}$$

The numerical integration in (7) is computed based on a cell-wise quadrature approach. The total physics loss $\mathcal{L}_{pde}$ aggregates these strong and weak residuals, as shown in (9):

$$\mathcal{L}_{pde} = \frac{1}{N}\sum_i \left(R_{r1}^2 + R_{r2}^2 + R_{r3,k}^i\right) \tag{9}$$

Finally, the total loss function integrates the data loss $\mathcal{L}_{ud}$ and physics loss $\mathcal{L}_{phys}$, defined as mean squared errors (MSE) between network predictions and known ground truths. N_p represents the number of data sampling points in each part:

$$\begin{aligned} \mathcal{L}_p &= \frac{1}{N_p}\sum_{i=1}^{N_p} |U(x_i, y_i, t_i) - U_{true}|^2 \\ p &\in \{ud, phys\} \end{aligned} \tag{10}$$

$$\mathcal{L}_{total} = \sum_p \lambda_p \mathcal{L}_p, \quad p \in \{ud, phys\} \tag{11}$$

B. M-BPINN architecture

A MPINN architecture is proposed to reduce spectral bias. It is observed that this bias is associated with high-gradient electromagnetic fields at the air gap and stator-rotor interfaces. Furthermore, periodic sinusoidal functions (SIREN) are utilized in the hidden layers to ensure that high-frequency features are accurately represented. The forward propagation for the l-th hidden layer is defined as:

$$h^l = \sin(\omega_0^l (W^l h^{l-1} + b^l)) \tag{12}$$

Where W^l and b^l denote the weight matrix and bias vector, ω_0^l represents the frequency hyperparameter. SIREN ensures non-vanishing, stable derivatives of all orders, which is critical for computing PDE residuals. To accurately characterize multi-scale spatial frequencies across multiple orders of magnitude, K parallel subnetworks $\{\phi_k\}_{k=1}^K$ are constructed. Each subnetwork applies a distinct discrete scaling factor s_k to the input z, as expressed in (13):

$$\phi_k(z) = \sigma_D \circ \sigma_{D-1} \circ \cdots \circ \sigma_1(s_k \cdot z), \quad k = 1, \ldots, K \tag{13}$$

Where σ_l denotes the SIREN hidden layer defined in (12). The extracted features from each parallel subnetwork are

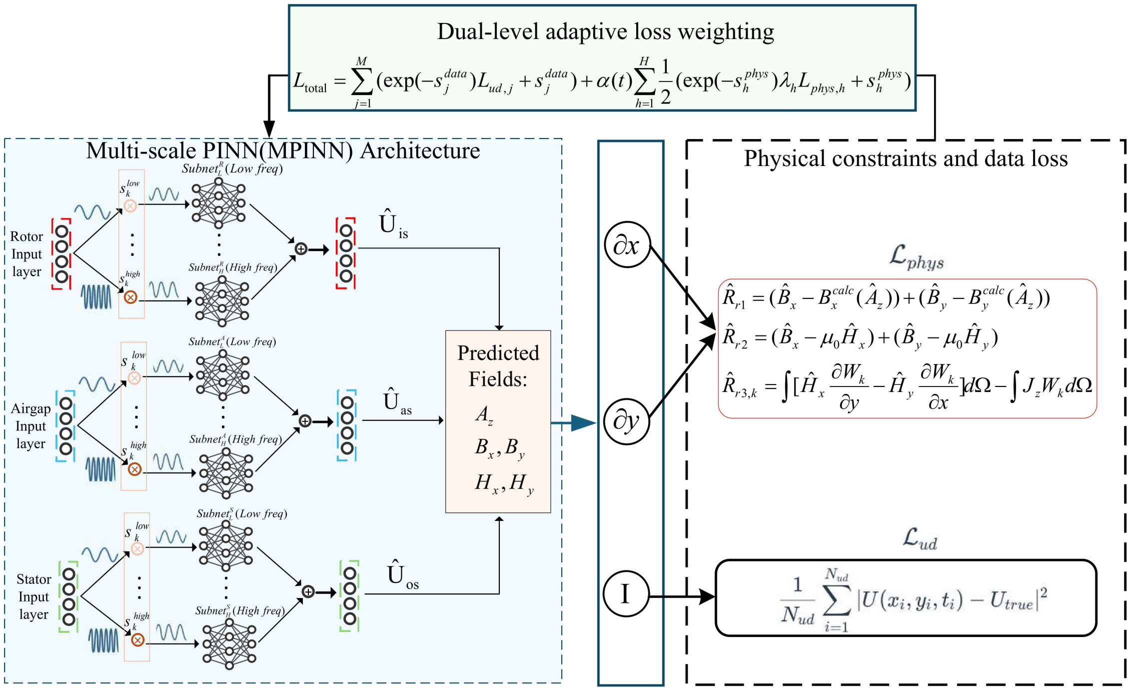

Fig. 1. Architecture of the proposed M-BPINN methodology.

cascaded at the output layer, and the system output is shown in (14):

$$U(z) = W_{out}[\phi_1(s_1 z); \phi_2(s_2 z); \dots; \phi_K(s_K z)] + b_{out} \quad (14)$$

Where $U = (A_z, B_x, B_y, H_x, H_y)^T \in \mathbb{R}^5$ is the normalized electromagnetic field output. This multi-scale architecture is applied independently to the rotor ($\mathcal{N}_{is}$), stator ($\mathcal{N}_{os}$), and air gap ($\mathcal{N}_{as}$) domains:

$$\begin{aligned} U_{is} &= \mathcal{N}_{is}(z_{is}; \Theta_{is}) \\ U_{os} &= \mathcal{N}_{os}(z_{os}; \Theta_{os}) \\ U_{as} &= \mathcal{N}_{as}(z_{as}; \Theta_{as}) \end{aligned} \quad (15)$$

Where z denotes the normalized inputs for each respective domain, and Θ represents the network parameters.

C. Dual-level adaptive loss weighting based on Bayesian uncertainty estimation

To address gradient pathology caused by disparate scales among physical fields and numerical noise from FEM interpolation, this noise is particularly evident around the complex geometric topology of PMSMs, such as air gap interfaces and stator teeth, where the magnetic field gradient is large, a dual-level adaptive loss weighting mechanism is proposed. The M data loss terms are balanced by a homoscedastic uncertainty framework in the first level. Assuming observation noise follows a Gaussian distribution with variance σ_j^2, the objective function via maximum likelihood estimation is shown in (16):

$$\mathcal{L}_{data} = \sum_{j=1}^{M} \left(\frac{1}{2\sigma_j^2} \mathcal{L}_{ud,j} + \log \sigma_j \right) \quad (16)$$

Where $\mathcal{L}_{ud,j}$ represents the unweighted MAE of the j-th specific data constraint. To ensure numerical stability and simplify the optimization process, a log-variance reparameterization method is used, (16) can be rewritten as:

$$\mathcal{L}_{data} = \sum_{j=1}^{M} \left(\exp(-s_j) \mathcal{L}_{ud,j} + s_j^{data} \right) \quad (17)$$

The learnable parameter s_j^{data} adaptively down-weights loss components with high errors to prevent gradient explosion, while the s_j^{data} regularization term penalizes excessive variance estimates. At the second level, a noise-aware adaptive mechanism is utilized to ensure that the impact of FEM interpolation errors on the H physical constraints is effectively reduced. Each constraint is assigned an independent learnable noise parameter $s_h^{phys} = \log \sigma_{phys,h}^2$, as shown in (18):

$$\mathcal{L}_{phys} = \sum_{h=1}^{H} \frac{1}{2} \left(\exp(-s_h^{phys}) \mathcal{L}_{phys,h} + s_h^{phys} \right) \quad (18)$$

This enables the network to automatically assess constraint difficulty at complex boundaries and adaptively reduce regularization strength to prevent overfitting. Combining the two stages, the system's total loss function is defined as:

$$\begin{aligned} \mathcal{L}_{total} = &\sum_{j=1}^{M} \left(\exp(-s_j^{data}) \mathcal{L}_{ud,j} + s_j^{data} \right) \\ &+ \alpha(t) \sum_{h=1}^{H} \frac{1}{2} \left(\exp(-s_h^{phys}) \lambda_h f(\mathcal{L}_{phys,h}) + s_h^{phys} \right) \end{aligned} \quad (19)$$

Where $\alpha(t)$ represents the physical constraint's asymptotic activation coefficient, λ_h represents the base physical weight, and $f(x) = \log(1 + x)$ is the dynamic range compression function. Finally, the Adam optimizer is employed alongside a standard cosine annealing learning rate schedule to ensure smooth decay and numerical stability.

III. FINITE ELEMENT MODELING AND M-BPINN CONSTRUCTION

In this study, a conical rotor permanent magnet synchronous motor (CR-PMSM) is modeled. M-BPINN is constructed utilizing electromagnetic field data generated via the FEA software Altair Flux 2020.

A. Finite Element Model of Conical Rotor Permanent Magnet Synchronous Motor

An 8-pole, 54-slot CR-PMSM is investigated in this study. A conical air-gap configuration featuring a 7° cone angle is adopted. The physical stator and rotor are depicted in Fig. 2, and the detailed geometric and material parameters of the motor are presented in Table I.

(a) (b) (c)

Fig. 2. Prototypes of the proposed CR-PMSM: (a) Stator iron core. (b) Rotor iron core. (c) The complete motor assembly.

TABLE I

GEOMETRIC AND MATERIAL PARAMETERS OF THE CR-PMSM

Parameter	Value	Parameter	Value
Number of poles	8	Stator outer diameter	130 mm
Number of slots	54	Stator inner diameter	86 mm
Number of pole pairs	4	Rotor outer diameter	85 mm
Cone angle	7°	Rotor inner diameter	53 mm
Rated speed	4000 rpm	Air-gap length	1 mm
Rated power	5.5 kW	Axial effective length	40 mm
Rated current	70.45 A	Permanent magnet material	NdFeB
Maximum current	200 A	Core material	Silicon steel

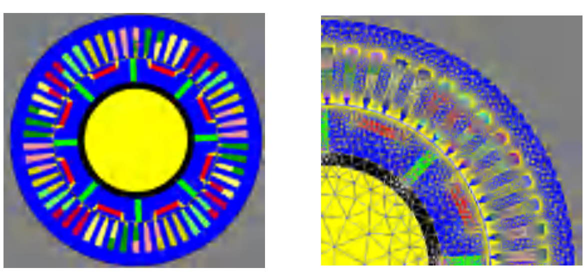

(a) (b)

Fig. 3. Finite element models of the CR-PMSM. (a) 2D cross-section. (b) One-quarter sector model.

A quarter-sector model of a 2D cross-section is developed for magnetostatic simulations by leveraging spatial periodic symmetry, as illustrated in Fig. 3. The computational domain is partitioned into three distinct regions. The rotor region comprises the permanent magnets and the rotor core, covering a radial range of 12.57–85.00 mm. Similarly, the stator region includes the stator core, 54 teeth/slots, and windings, with a radial span of 86.00–130.00 mm. The air-gap region is represented by the midline at $r = 85.49$ mm. Static solutions are computed for 46 rotor positions, where the angle θ varies from $0°$ to $90°$ in increments of $2°$.

B. Dataset Composition and Division

Due to the equipment constraints of the experimental testbed, the maximum motor speed is limited to 2000 r/min. The operating conditions are set at 2000 r/min, 70.45 A rated current, and a current angle γ of $110.5°$. Steady-state simulations yield a total of 4,519,973 spatial node data points. A random sampling strategy is implemented to ensure that 15% of the data points per angle are selected for dataset construction, resulting in 677,996 points across 46 angles. The allocation of the dataset is presented in Table II.

TABLE II

DETAILED SCHEME OF DATASET PARTITIONING

Domain	Training Set (37θ)	Validation Set (5θ)	Test Set (4θ)	Total
Rotor	96,048	10,672	10,672	117,392
Stator	440,676	48,964	48,964	538,604
Air-gap	18,000	2,000	2,000	22,000
Total	554,724	61,636	61,636	677,996

The training set consists of 37 angle groups. The validation set corresponds to $\theta \in \{14°, 20°, 44°, 68°, 84°\}$ for hyperparameter selection and early stopping. The test set comprises $\theta \in \{10°, 30°, 60°, 80°\}$, with angles uniformly distributed and mutually exclusive from the training set. The distribution of this test set ensures that interpolation capabilities are evaluated. The angle selection strategy aligns with the electromagnetic principles of the 8-pole (4-pole pair), 54-slot motor. The 0°–90° mechanical angular domain maps exactly to a complete $360°$ electrical period. The angles $\theta = 10°$ and $\theta = 80°$ (corresponding to electrical angles of $40°$ and $320°$) are located near the boundaries of this period. These positions test the capacity of the model to capture fringing field effects and local saturation between the stator and the rotor. The angles $\theta = 30°$ and $\theta = 60°$ (corresponding to $120°$ and $240°$ electrically) represent typical phase characteristic points in a three-phase system. These points characterize intermediate transition states that exhibit intense flux path shifts inside the stator teeth and yoke. This comprehensive test set evaluates the generalization performance of the neural network under the specified operating conditions.

C. M-BPINN Construction and Training

The proposed M-BPINN was trained on an NVIDIA GeForce RTX 5090 GPU using PyTorch. Independent subnetworks are constructed for the rotor, stator, and air-gap domains. Each subnetwork consists of five SIREN hidden layers with $\omega_0 = 20.0$ and input scaling factors $\{1, 2, 4, 8, 16, 32\}$. The stator subnetwork employs 512-dimensional hidden layers, while the rotor and air-gap subnetworks use 128 dimensions. Input coordinates are subjected to global z-score normalization; output fields are normalized per domain. Standard MSE is applied to A_z, while Smooth L1 loss ($\beta = 0.1$) is used for B and H. All physical constraint losses employ learnable $\log \sigma^2$ parameters for adaptive weighting The network is trained using the Adam optimizer for 8,000 epochs with an initial learning rate of 1×10^{-3} and a cosine annealing scheduler, and the physical constraints activated from epoch 1800.

IV. RESULTS AND DISCUSSION

This section systematically evaluates the predictive accuracy of the proposed M-BPINN. Firstly, an overall analysis of the predictive accuracy is provided in Section IV-A. Subsequently, the convergence behavior of the individual loss terms during training and the effectiveness of the physical constraints are discussed in Section IV-B.

A. Analysis of Overall Prediction Accuracy

The predictive capability of the proposed M-BPINN model is evaluated by comparing predicted results with the full-domain FEA reference solution, using an independent test set of rotor angles $\theta \in \{10°, 30°, 60°, 80°\}$.

As shown in Table III and Table IV, the RelMAE of A_z in all fields is below 2.5%. For B and H, the gradual increase in geometric and material complexity is reflected from an air gap accuracy of around 7% to a rotor accuracy of 8%–13% and a stator accuracy of 12%–13%. The maximum error is concentrated at the slot-tooth boundary and the edge of the permanent magnet, consistent with the high-gradient field region.

TABLE III
PREDICTION ERRORS FOR EACH DOMAIN AND FIELD QUANTITY ON THE TEST SET ($\theta \in \{10°, 30°, 60°, 80°\}$)

Domain	Field	MAE	RelMAE%	MaxAE
Rotor	A_z	1.852e-04	1.93	1.037e-03
	B_x	5.863e-02	7.87	2.806e+00
	B_y	5.753e-02	7.71	2.795e+00
	H_x	2.120e+03	12.50	1.081e+05
	H_y	2.279e+03	13.17	1.358e+05
Stator	A_z	2.300e-04	2.21	1.728e-03
	B_x	4.492e-02	12.62	1.399e+00
	B_y	4.520e-02	12.82	1.403e+00
	H_x	4.966e+02	12.51	9.650e+04
	H_y	4.905e+02	12.32	1.380e+05
Air gap	A_z	1.760e-04	1.65	1.404e-03
	B_x	2.468e-02	7.10	1.805e-01
	B_y	2.430e-02	7.02	2.548e-01
	H_x	1.968e+04	7.11	1.430e+05
	H_y	1.935e+04	7.02	2.035e+05

TABLE IV
SUMMARY OF KEY ERROR METRICS AND COMPUTATIONAL TIME

Domain (Test Points)	B avg RelMAE%	H avg RelMAE%	A_z RelMAE%
Rotor (10,672)	7.79	12.84	1.93
Stator (48,964)	12.72	12.42	2.21
Air gap (2,000)	7.06	7.07	1.65

Runtime at $\theta = 30°$: FEM, 753 s; M-BPINN, 0.56 s; speedup, 1.35×10^3.

Electromagnetic field predictions at $\theta = 30°$ are illustrated in Fig. 4. This figure provides a comprehensive comparison among the FEA reference solutions, the M-BPINN predictions, and the point-wise absolute errors. It is demonstrated that the M-BPINN accurately captures the periodic magnetic pole structures and the tooth-tip magnetic flux density. The prediction errors are mainly concentrated at the stator slot-tooth boundaries and the rotor magnet edges, where high-frequency spatial gradients and material discontinuities are present in these specific areas. In terms of efficiency, M-BPINN inference requires only 0.56 s compared to 753 s for FEM, achieving a three-order-of-magnitude acceleration suitable for real-time digital twins.

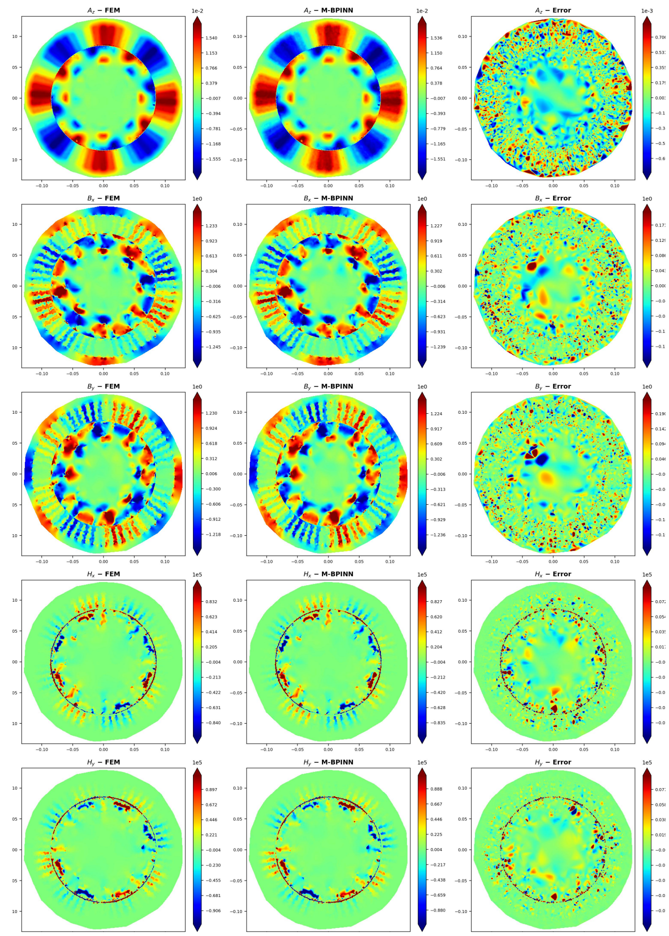

Fig. 4. Electromagnetic field prediction results at $\theta = 30°$. Left column: FEA reference solution; middle column: M-BPINN prediction; right column: point-wise absolute error.

B. Analysis of the Training Process and the Validity of Physical Constraints

The training convergence comparison in Figure 5(a) shows that the purely data-driven model (MNN) and the fixed-weight model (M-PINN) both suffer from early-stage plateauing or objective competition, whereas the proposed M-BPINN achieves improved convergence efficiency and the lowest final error. This demonstrates the effectiveness of Bayesian adaptive weighting in resolving multi-objective optimization conflicts

The effectiveness of the physical constraints is quantified utilizing the weighted validation loss $\mathcal{L}_{wval}$. A rapid reduction in loss is observed during the initial data phase (epochs 0–1800), which is subsequently followed by a period of stagnation, as illustrated in Fig. 5(b). The progressive activation of physical constraints (epochs 1800–4200) ensures that the loss reaches a final value of 0.00278. This result constitutes a 73.9% reduction relative to the data-only baseline. Both data and physical losses exhibit a monotonically decreasing trend

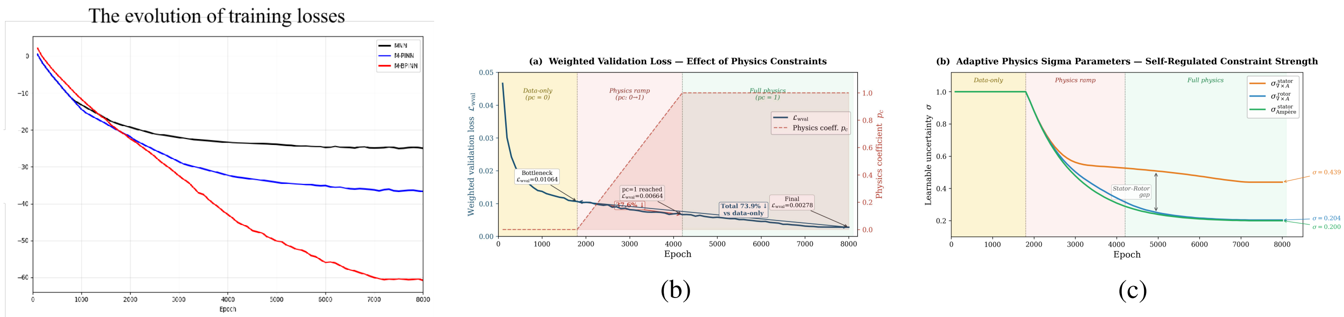

(a) (b) (c)

Fig. 5. Analysis of training dynamics. (a) Training loss convergence comparison among MNN, M-PINN, and M-BPINN. (b) Weighted validation loss and physical constraint activation coefficient. (c) Evolution of learnable physics σ parameters.

following constraint activation. This phenomenon indicates that destructive interference between objectives is reduced by the synergistic effect of the progressive activation strategy and the Bayesian adaptive weighting.

Furthermore, the self-regulating nature of the learnable σ parameter is revealed in Fig. 5(c). A higher uncertainty value is assigned by the network to the complex stator region ($\sigma = 0.439$) compared to the rotor ($\sigma = 0.204$). Consequently, the weight of difficult constraints is automatically reduced to ensure that over-regularization in high-gradient areas is prevented.

V. Conclusions

This article proposes an M-BPINN architecture for predicting the global electromagnetic response of PMSMs at different rotor positions. This architecture combines SIREN based multi-scale subnetworks with discrete scaling factors to reduce spectral bias. Consequently, the magnetic vector potential, magnetic flux density, and magnetic field intensity across the rotor, stator, and air-gap domains are accurately approximated. Furthermore, a dual-level adaptive loss weighting mechanism based on Bayesian uncertainty estimation is proposed. Learnable σ parameters automatically accommodate the varying constraint satisfaction difficulty across distinct geometric regions to balance data and physical residuals. The analysis results demonstrate that M-BPINN achieves relative mean absolute errors (RelMAEs) below 2.5% for A_z and 7%–13% for B and H under unknown operating conditions; compared to the data-only baseline, the validation loss is reduced by 73.9%. In addition, the proposed method achieves a three-order-of-magnitude computational acceleration over the FEA, As summarized in Table IV, for the same $\theta = 30°$ test case, FEM required 753 s, whereas trained M-BPINN inference required only 0.56 s.

References

[1] F. Un-Noor, S. Padmanaban, L. Mihet-Popa, M. N. Mollah, and E. Hossain, "A comprehensive study of key electric vehicle (ev) components, technologies, challenges, impacts, and future direction of development," *Energies*, vol. 10, no. 8, p. 1217, 2017.

[2] Y. Fan, P. Liang, L. Liang, D. Zhang, W. Liu, and X. Zhang, "Analytical model of no-load axial force for electric propulsion conical motor in electric aircraft," *IET Electric Power Applications*, vol. 18, no. 3, pp. 336–344, 2024.

[3] J. Wang, S. Huang, C. Guo, and Y. Feng, "Magnetic field and operating performance analysis of conical-rotor permanent magnet synchronous motor," *CES Transactions on Electrical Machines and Systems*, vol. 2, no. 1, pp. 181–187, 2018.

[4] X. Liang, M. Z. Ali, and H. Zhang, "Induction motors fault diagnosis using finite element method: A review," *IEEE Transactions on Industry Applications*, vol. 56, no. 2, pp. 1205–1217, 2019.

[5] M. Nazem and M. H. Moavenian, "Alternative remeshing techniques for large deformation analysis of geotechnical problems," *Computers and Geotechnics*, vol. 138, p. 104344, 2021.

[6] K. Hornik, M. Stinchcombe, and H. White, "Multilayer feedforward networks are universal approximators," *Neural networks*, vol. 2, no. 5, pp. 359–366, 1989.

[7] F. J. Montáns, F. Chinesta, R. Gómez-Bombarelli, and J. N. Kutz, "Data-driven modeling and learning in science and engineering," *Comptes Rendus Mécanique*, vol. 347, no. 11, pp. 845–855, 2019.

[8] Y. Dong, H. Jiang, M. Mu, and X. Wang, "A trustworthy lightweight multi-expert wavelet transformer for rotating machinery fault diagnosis," *Mechanical Systems and Signal Processing*, vol. 235, p. 112945, 2025.

[9] S. Cuomo, V. S. Di Cola, F. Giampaolo, G. Rozza, M. Raissi, and F. Piccialli, "Scientific machine learning through physics–informed neural networks: Where we are and what's next," *Journal of Scientific Computing*, vol. 92, no. 3, p. 88, 2022.

[10] M. Raissi, P. Perdikaris, and G. E. Karniadakis, "Physics-informed neural networks: A deep learning framework for solving forward and inverse problems involving nonlinear partial differential equations," *Journal of Computational physics*, vol. 378, pp. 686–707, 2019.

[11] S. Son, H. Lee, D. Jeong, K.-Y. Oh, and K. H. Sun, "A novel physics-informed neural network for modeling electromagnetism of a permanent magnet synchronous motor," *Advanced Engineering Informatics*, vol. 57, p. 102035, 2023.

[12] J. Gao, W. Gui, X. Xie, R. Wan, S. Yin, and C. Yang, "Temperature-insensitive irreversible demagnetization fault diagnosis based on dual-state flux estimation for pmsm," *IEEE Transactions on Power Electronics*, 2025.

[13] Z. Wu, S. Zuo, S. Hu, and X. Hu, "Analytical modelling of air-gap magnetic field of interior permanent magnet synchronous motors," *IET Electric Power Applications*, vol. 14, no. 11, pp. 2101–2110, 2020.

[14] N. Rahaman, A. Baratin, D. Arpit, F. Draxler, M. Lin, F. Hamprecht, Y. Bengio, and A. Courville, "On the spectral bias of neural networks," in *International conference on machine learning*. PMLR, 2019, pp. 5301–5310.

[15] S. Wang, Y. Teng, and P. Perdikaris, "Understanding and mitigating gradient flow pathologies in physics-informed neural networks," *SIAM Journal on Scientific Computing*, vol. 43, no. 5, pp. A3055–A3081, 2021.

[16] S. Wang, X. Yu, and P. Perdikaris, "When and why pinns fail to train: A neural tangent kernel perspective," *Journal of Computational Physics*, vol. 449, p. 110768, 2022.

[17] L. D. McClenny and U. M. Braga-Neto, "Self-adaptive physics-informed neural networks," *Journal of Computational Physics*, vol. 474, p. 111722, 2023.

[18] L. Lu, R. Pestourie, W. Yao, Z. Wang, F. Verdugo, and S. G. Johnson, "Physics-informed neural networks with hard constraints for inverse design," *SIAM Journal on Scientific Computing*, vol. 43, no. 6, pp. B1105–B1132, 2021.